

Single-Crystalline Rutile TiO_2 Hollow Spheres: Room-Temperature Synthesis, Tailored Visible-Light-Extinction, and Effective Scattering Layer for Quantum Dot-Sensitized Solar Cells

Hongqiang Wang,^{*,†,‡} Masahiro Miyauchi,[†] Yoshie Ishikawa,[§] Alexander Pyatenko,[†] Naoto Koshizaki,^{*,†} Yue Li,^{†,‡} Liang Li,^{||,‡} Xiangyou Li,[†] Yoshio Bando,^{||} and Dmitri Golberg^{||}

[†]Nanosystem Research Institute (NRI), National Institute of Advanced Industrial Science and Technology (AIST), Central 5, 1-1-1 Higashi, Tsukuba, Ibaraki 305-8565, Japan

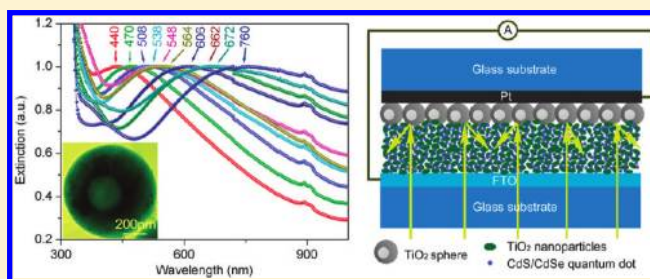
[‡]Key Laboratory of Materials Physics, Anhui Key Laboratory of Nanomaterials and Nanotechnology, Institute of Solid State Physics, Chinese Academy of Sciences, Hefei 230031, People's Republic of China

[§]Department of Advanced Materials Science, Faculty of Engineering, Kagawa University, Japan

^{||}International Center for Materials Nanoarchitectonics (MANA), National Institute for Materials Science (NIMS), Namiki 1-1, Tsukuba, Ibaraki 305-0044, Japan

S Supporting Information

ABSTRACT: A general synthesis of inorganic single-crystalline hollow spheres has been achieved through a mechanism analogous to the Kirkendall effect, based on a simple one-step laser process performed at room temperature. Taking TiO_2 as an example, we describe the laser process by investigating the influence of experimental parameters, for example, laser wavelength, laser fluence/irradiation time, liquid medium, and concentration of starting materials, on the formation of hollow spheres. It was found that the size-tailored TiO_2 hollow spheres demonstrate tunable light scattering over a wide visible-light range. Inspired by the effect of light scattering, we introduced the TiO_2 hollow sphere's scattering layer in quantum dot-sensitized solar cells and achieved a current notable 10% improvement of solar-to-electric conversion efficiency, indicating that TiO_2 hollow spheres are potential candidates in optical and optoelectronic devices.



INTRODUCTION

Systematic control over the assembly of inorganic nanoparticles into superstructures at microscale and nanoscale levels has recently attracted great interest due to the amazing versatility of such materials.¹ As a unique micro-/nanostructure, hollow spheres with specific features (e.g., low density, high surface-to-volume ratio, and the effect of void space) have been used in many important applications (e.g., catalysis, drug delivery, lithium-ion batteries, solar cells, and controlled release of various substances).² Many methods have been developed for preparing hollow spheres, and they usually require removable or sacrificial templates that are hard (e.g., monodispersed polymer latex, carbon, silica spheres, and reduced metal nanoparticles)³ or soft (e.g., micelles, microemulsions, macromolecules, oil droplets, and gas bubbles)⁴ to direct the formation of inorganic nanoparticles on their surfaces by adsorption or chemical reactions. Recently, a number of template-free methods for generating hollow inorganic microstructures and nanostructures have been developed using Ostwald ripening and Kirkendall diffusion.⁵ Thanks to the efforts contributed by many groups, a variety of hollow spheres could be acquired in a delicately controlled manner. However, seeking simple approaches that

enable the general fabrication of hollow inorganic spheres is still a challenge.

As an important semiconductor, titanium dioxide (TiO_2) has been extensively investigated for a vast range of applications (e.g., photocatalysis, solar cells/batteries, field emission, and self-cleaning), due to its peculiar chemical and physical properties.^{1b,2c,6} Recently, major research appears to be shifting to create TiO_2 hollow spheres, because they have been evaluated as attractive candidates for sensors, lithium storage, lithium-ion batteries, solar cells, and photocatalysts.^{2c,7} Thus far, TiO_2 hollow structures have been built mostly by subunits of nanoparticles,^{2c,7} thus present as polycrystalline or amorphous throughout the spheres, which might influence or even reduce their performance in optical, electrical, and optoelectronic applications, due to poor crystal quality and insufficiently close contact between subunits.

In the present study, we demonstrate a one-step laser process for constructing size-tailored TiO_2 hollow spheres, through a mechanism analogous to the Kirkendall effect. It is noteworthy

Received: May 30, 2011

Published: October 24, 2011

that single-crystalline hollow spheres are produced with this process due to unique pulsed laser heating, even though the experiment is performed at room temperature. The size-tailored hollow spheres demonstrate tunable light scattering over a wide visible-light range. Inspired by the effect of light scattering, we introduced the TiO₂ hollow sphere's scattering layer in quantum dot-sensitized solar cells (QDSSCs) and achieved a notable 10% improvement of solar-to-electric conversion efficiency. The wide-range size-related extinction and improved efficiency by light scattering in solar cells indicate that TiO₂ hollow spheres are potential candidates in optical and optoelectronic devices. Importantly, this method has been found suitable for fabricating other size-tailored semiconductor hollow spheres, which could pave the way for the extensive studies on single-crystalline inorganic hollow spheres.

EXPERIMENTAL SECTION

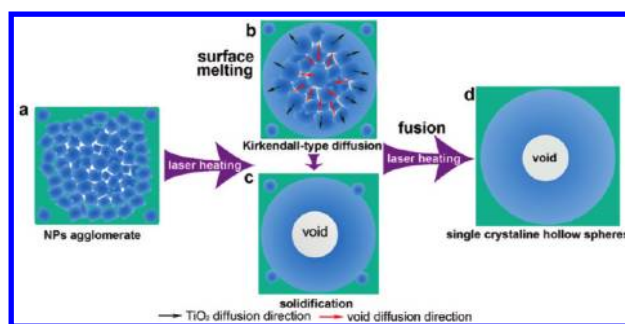
Materials Synthesis. An Nd:YAG laser (Quanta Ray from Spectra-Physics; pulse width 10 ns, repetition rate 30 Hz) was used as the light source for pulsed laser irradiation. Typically, 1 mg of commercial TiO₂ nanoparticles (Aldrich, 25 nm, powder form) was first well dispersed in 4 mL of acetone (99.5%, Wako) by ultrasonic vibration. The mixture was then transferred to a sealed reaction cell and irradiated by an unfocused laser beam (133 mJ/pulse·cm², third harmonic) for 30 min. After laser irradiation, the powder collected by centrifugation was washed several times with diluted aqueous HCl solution (3.5 wt %) and recollected.

To investigate the effect of laser fluence and laser irradiation time on size evolution, TiO₂ colloidal nanoparticles in acetone (0.2 mg/mL) were irradiated by an unfocused laser beam (67, 83, 100, 117, 133 mJ/pulse·cm², third harmonic) for 20 and 30 min. To investigate the influence of liquid medium on the formation of spherical particles, TiO₂ colloidal nanoparticles in water (Millipore, 0.2 mg/mL) were irradiated by an unfocused laser beam (133 mJ/pulse·cm², third harmonic) for 20 min. To determine the effect of raw material concentration on the formation of spherical particles, an unfocused third-harmonic laser (133 mJ/pulse·cm²) was used to irradiate TiO₂ colloidal nanoparticles in acetone (99.5%, Wako) with different concentrations (0.0625, 0.125, 0.25, 0.5, and 1 mg/mL).

Characterization. The phase, morphology, and microstructure of the collected particles were measured and observed using a powder diffractometer (Rigaku; Ultima IV/PSK), field-emission scanning electron microscope (FESEM, Hitachi S4800) and transmission electron microscopy (TEM, JEOL 2010). Dynamic light scattering (DLS) measurement of spherical particles with different sizes was performed by Malvern Zetasizer Nano ZS (Malvern, Herrenberg, Germany), and Dispersion Technology Software version 4.20 from Malvern was used to collect and analyze the data. The optical extinction properties of suspensions with dispersed TiO₂ submicrometer spheres in acetone were evaluated using a UV-vis spectrophotometer (Shimadzu UV-2100PC).

Solar Cell Construction and Characterization. Mesoporous TiO₂ film of 10 μm thickness and 5 × 5 mm² area was prepared by commercially screen-printing the paste of TiO₂ nanoparticles onto the FTO glass substrates, followed by annealing at 500 °C for 1 h. The SiO₂-modified CdS/CdSe-QDs cosensitized TiO₂ films were prepared following ref 8. Briefly, for the CdS/CdSe QDs cosensitized electrodes, CdS QDs were first deposited on the TiO₂ films by repeating five times of separately immersing TiO₂/FTO into aqueous solutions of Na₂S (0.1 M) and CdSO₄ (0.1 M), and then CdSe QDs were deposited for 5 h in a chemical bath containing 0.5 M CdSO₄, 0.7 M sodium nitrilotriacetate, 0.2 M Na₂SeSO₃ with pH value of 11 adjusted by NaOH (0.1 M), and subsequently a SiO₂ thin layer was coated on the QDs-sensitized TiO₂

Scheme 1. Schematic Illustration of Single-Crystalline TiO₂ Hollow Sphere Formation by Bottom-Up Laser Processing



film by dipping the sample in tetraethyl orthosilicate ethanol solution (0.208 g/10 mL) for 15 min. Finally, scattering layers of TiO₂ spheres (prepared in acetone, 133 mJ/pulse·cm², third harmonic, 30 min, 0.2 mg/mL) were prepared by dropping different volumes of concentrated TiO₂ colloidal aqueous solution (2.625 mg/mL) onto the QD-sensitized TiO₂ mesoporous film electrode (from 6 to 26.7 μL), followed by natural drying. A square mask with a central hollow area of 5 × 5 mm² was used to keep the dropped solution naturally drying on the surface of the QD-sensitized TiO₂ mesoporous film electrode.

The QD-sensitized photoanodes were sealed in a sandwich cell with a 30 μm spacer by using Pt-coated FTO glass as a counter electrode. Polysulfide aqueous solution containing 0.5 M Na₂S, 0.125 M S, and 0.2 M KCl was used as an electrolyte. Electrical characteristics and photovoltaic properties of each solar cell were measured using simulated AM1.5 sunlight illumination at 100 mW cm⁻². The light source was an Ultraviolet Solar Simulator (model 16S, Solar Light Co., Philadelphia, PA) with a 200 W xenon lamp power supply (model XPS 200, Solar Light Co., Philadelphia, PA).

RESULTS AND DISCUSSION

Scheme 1 illustrates the construction of single-crystalline hollow spheres by pulsed laser irradiation of colloidal nanoparticles (PLICN) of TiO₂ at room temperature. Because of the ultrasmall size of TiO₂ nanoparticles (25 nm), the nanoparticles are strongly agglomerated to form larger congeries. After the solid particles are dispersed into the liquid, the liquid will penetrate into the agglomerate and compress the air inside, and this pressured air acts against further liquid moving in. On the other hand, numerous nanoscaled spaces among nanoparticles within the agglomerate will form a nanochannel for the liquid molecules diffusion, and the resulted capillary forces probably do not allow the deep diffusion of liquid molecules into the inner part of the agglomerate. Therefore, abundant voids are considered to exist inside the agglomerates after dispersing them in liquid (Scheme 1a). Once the TiO₂ congeries absorb enough laser energy upon pulsed laser irradiation, the temperature of out particles in congeries will increase above the melting point in a very short time (on the order of nanoseconds). Because the heat transfer is not as rapid as the energy absorption process, the process of particles' melting will start first at the surface of agglomerate and then propagate to the center. Upon the very short time laser heating, we will have the liquid layer around not yet melted particles in the center. This liquid layer will capture the air inside the agglomerate during its further melting process (Scheme 1b). Meanwhile, the volumes of inner separated voids are dramatically expanded due to the fast temperature increase,

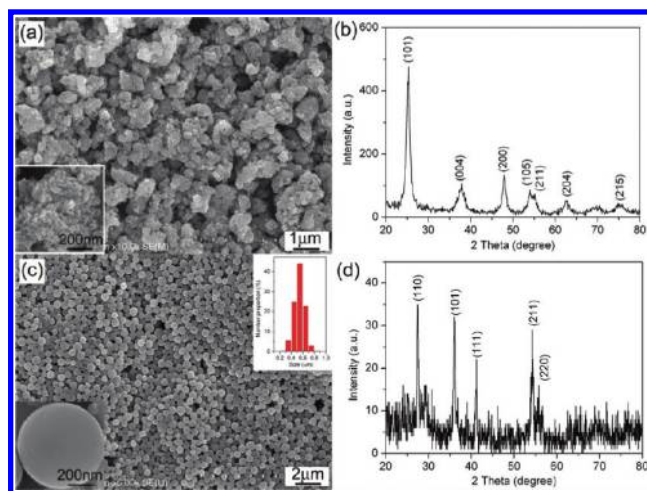


Figure 1. (a) FESEM image and (b) XRD pattern of TiO₂ raw nanoparticles. (c) FESEM image and (d) XRD pattern of TiO₂ spherical particles by PLICN (355 nm, 133 mJ/pulse · cm², 30 min, in acetone). Insets in (a) and (c) are FESEM images of highlighted single congeries and spherical particle.

forcing inner nanoparticles to approach the melted surface. To reduce the surface energy, the separated voids will gradually merge to form one larger void (Scheme 1c). After that, molten particles are cooled by the surrounding liquid medium, during which the particles recrystallize.⁹ Because of the unique selective pulsed heating,¹⁰ the congeries surface quickly melts, and the shape transforms from irregular to spherical. This process is similar to that of the Kirkendall effect^{5a} and can be schematically described in Scheme 1b and c: TiO₂ nanoparticles diffuse outward, due to the melting of the whole sphere by continuous laser heating, while there is balancing inward flow of vacancies, finally forming a stable solid/gas interface. After numerous pulsed-heating cycles, the sphere will grow up by fusion with nearby nanospheres and recrystallize into a single crystalline hollow sphere (Scheme 1d).

Figure 1 compares raw material and the final product by PLICN of TiO₂. A FESEM image of commercial TiO₂ nanoparticles (Aldrich, 25 nm) is presented in Figure 1a, where the nanoparticles are strongly agglomerated. The highlighted single congeries of nanoparticles is depicted in the inset of Figure 1a. The corresponding X-ray diffraction (XRD) pattern (Figure 1b) indicates that the raw nanoparticles have an anatase phase (JCPDS card no. 21-1272), and the relatively broad width of the diffraction peaks reveals the small size of the nanoparticles. Irradiating the raw nanoparticles dispersed in acetone for 30 min using a 355 nm laser (133 mJ/pulse · cm²) produced many spherical particles (Figure 1c). A FESEM image of a 500 nm single particle (left inset of Figure 1c) reveals its spherical shape and smooth surface, which is morphologically different from those constructed by nanoparticles.^{2c,7} A histogram plotted by analyzing more than 400 particles (right inset of Figure 1c) indicates that the resultant spherical particles have an average size of 540 nm. The XRD pattern of these particles is depicted in Figure 1d, and it can be observed that the phase of the products becomes rutile after laser irradiation (JCPDS card no. 2-494). The obviously decreased diffraction peak width (Figure 1d) as compared to that of raw material (Figure 1b) structurally indicates that the resultant spheres are no longer constructed with nanoparticle subunits.

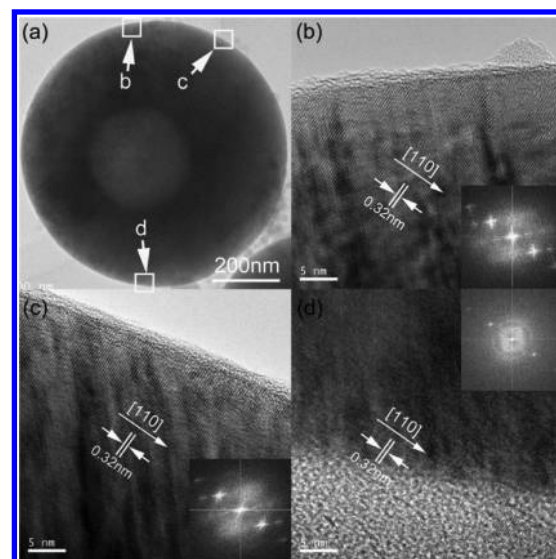


Figure 2. (a) TEM image of a single TiO₂ hollow sphere. (b–d) HRTEM images and corresponding fast Fourier transform patterns (insets) of the areas labeled in (a).

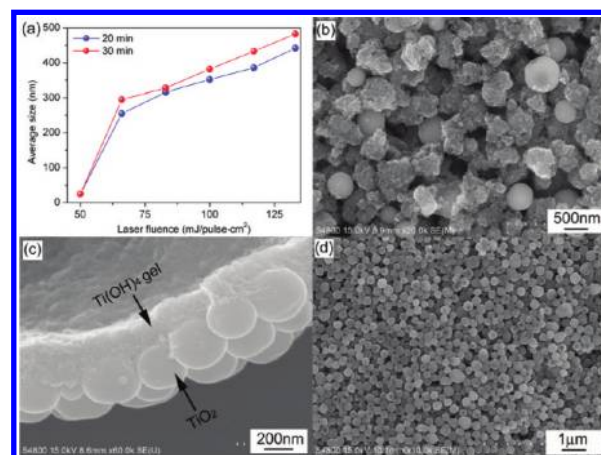


Figure 3. (a) Laser fluence/irradiation-time-dependent size change of products by PLICN. (b) Typical FESEM image of a product by PLICN in acetone using 532 nm laser (20 min, 333 mJ/pulse · cm²). (c) FESEM image of a product formed by PLICN in water using 355 nm laser (10 min, 133 mJ/pulse · cm²). (d) FESEM image of a product formed by PLICN in acetone using 355 nm laser (1 mg/mL, 20 min, 133 mJ/pulse · cm²).

TEM was used to further investigate the microstructures of the resultant spherical particles. Interestingly, these spherical particles are mainly hollow structures (Figure S1), and the hollow parts of the spheres are always randomly situated, rather than being centrally located (Figure 2a). Because the spherical particles are several hundreds of nanometers in size, we can observe only the high-resolution TEM (HRTEM) image of their edges. The lattice fringes from the edge of the spheres (Figure 2b) correspond to the interplanar *d*-spacing of rutile TiO₂ (110). The clear lattice fringes and the corresponding fast Fourier transform pattern depicted in the inset of Figure 2b indicate the single crystalline nature of the resultant TiO₂ hollow spheres. We randomly checked several points of the edge of the hollow sphere, and coherent fast Fourier transform

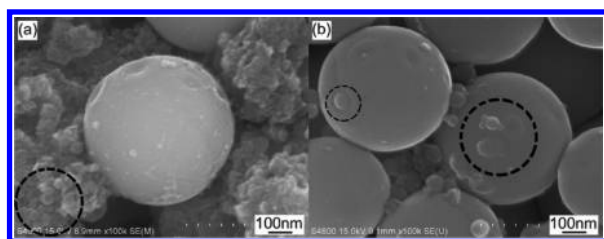


Figure 4. FESEM images of products by PLICN of TiO_2 with different irradiation times (0.2 mg/mL, 355 nm, 133 mJ/pulse \cdot cm^2). (a) 1 min. (b) 10 min. The labeled area in (a) indicates sphere formation from isolated nanoparticles. The labeled areas in (b) indicate the fusion of isolated nanospheres with submicrometer spheres.

patterns and lattice fringes (Figure 2c and d) confirmed its single crystalline feature.

Further study reveals that we can easily control the sizes of the resultant TiO_2 spherical particles by simply tuning the input laser fluence. Figure 3a illustrates the laser fluence-dependent size evolution of the TiO_2 spherical particles, where the average sizes of the particles are recorded from dynamic light scattering (DLS) measurement. Because no morphological change is observed after the laser irradiation of TiO_2 nanoparticles using a fluence of 50 mJ/pulse \cdot cm^2 (Figure S2), we assume the average particle size is 25 nm, the same as that of raw nanoparticles. Irradiating with a 355 nm laser (67–133 mJ/pulse \cdot cm^2) for 20 min results in spherical particles with an average size ranging from 255 to 442 nm. When other conditions are unchanged and the irradiation time is extended to 30 min, the sizes of the obtained spherical particles range from 295 to 483 nm, a slight increase over those irradiated for 20 min. This fluence/time-dependent size increase is in agreement with our previous studies.¹¹

The adopted laser wavelength, liquid medium, and raw nanoparticles concentration also influence the synthesis of TiO_2 spherical particles. With a 355 nm laser, even low laser fluence (e.g., 67 mJ/pulse \cdot cm^2) can result in the formation of spherical particles. However, with a 532 nm laser, only fluence exceeding 333 mJ/pulse \cdot cm^2 can lead to the formation of TiO_2 spheres (Figure 3b). This is reasonable when one considers the band gap of TiO_2 , which is 3.2 eV for anatase and is thus favorable for the absorption of UV laser (355 nm). We also performed laser irradiation in pure water. After dropping and drying the resultant colloidal solution on a silicon wafer, we always obtained a thin layer covering the spheres (Figure 3c). This thin layer is assumed to be titanium hydroxide gel because it is easily formed during laser irradiation when the solvent contains a certain amount of water.¹² This thin gel layer can be removed by diluted HCl solution (3.5 wt %, Figure S3). Therefore, even with highly pure acetone, the obtained TiO_2 spheres still need HCl washing due to the small amount of water in acetone. The concentration of raw nanoparticles also affects the morphology of the spherical particles. With increased concentration, spherical particle size increases. However, when we used a raw colloidal solution with a much higher concentration (e.g., 1 mg/mL, see Figure 3d), irregular non-spherical structures that seemed to result from particle fusion were always produced.

In experiments conducted with a Nd:YAG laser, the heating–melting–evaporation mechanism is responsible for the size change.¹³ If a nanoparticle absorbs sufficient laser beam energy, it melts and/or evaporates. With high enough input laser fluence, the temperature of TiO_2 nanoparticles dispersed in solvent rises

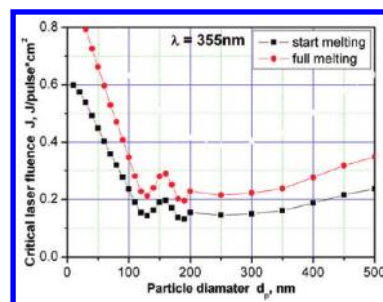


Figure 5. Particle size dependence of the required laser fluence J for anatase TiO_2 to heat an individual spherical particle to the melting point (start melting) and to full melting, using the pulsed laser (355 nm).

dramatically, up to the melting point, due to absorption of the laser-beam energy, and the resultant particles are believed to exist in the form of spherical liquid droplets.¹⁴ At temperature exceeding the melting point, TiO_2 nanoparticles recrystallize into rutile phase, a high-temperature stable phase. After pulsed heating (within 10 ns), quenching occurs, usually in less than 10^{-4} s.^{13b,15} Such rapid cooling helps inhibit the reorientation of surface atoms on a spherical particle, thus maintaining the spherical shape; that is why spherical particles can be formed with our technique. In addition, fast quenching helps maintain the high temperature rutile phase.

Actually, separate nanoparticles always exist together with agglomerates. Both large agglomerates and isolated nanoparticles are melted completely to form spherical particles when enough energy is absorbed from the pulsed laser (Figure 4a). After continuous laser irradiation, the nearby melted nanospheres fuse together and then remelt into a sphere with a size increase (Figure 4b).

As described above, the laser power, laser wavelength, starting particles concentration, and dispersion media were found experimentally influence the formation of spherical particles. All theoretical calculations were made for individual spherical particles of different diameter in our study; we assume that all laser energy absorbed by the particle will be spent on heating the nanoparticles, leading to the start melting, full melting, start evaporation, and full evaporation of the particles,¹⁰ in which for the first approximation we do not consider some secondary effects like possible pyrolysis of solvent around a particle and interaction of product of this pyrolyzed product with particle surface. As described in eq 1, the required laser energy Q_{abs} for particles of different sizes, which will heat a particle from T_0 (298.15 K) to the melting point T_m (starting melting), to complete melting (plus melting heat), can be determined. Herein, we define start melting as the melting of particles surface, while full melting is melting of the whole particle. Once the whole particle is full melted, we believe that its shape is spherical, which could be retained after the fast quenching process. Therefore, spherical particles we finally obtain are those full-melted during laser irradiation. The physical and thermodynamic constants used in eq 1, that is, the density ρ_p , the heat capacities C_p^s for solid, and the melting heat ΔH_m , were adopted from JANAF.¹⁶

$$Q_{\text{abs}} = \rho_p (\pi d^3 / 6) \{ C_p^s (T_m - T_0) + \Delta H_m \} \quad (1)$$

On the other hand, the absorbed laser energy by the spherical particles with the size d_p can be determined by eq 2, in which J is the laser fluence, and $\sigma_{\text{abs}}^\lambda$ is the absorption cross section. We used Mie theory to calculate the absorption cross section $\sigma_{\text{abs}}^\lambda$,

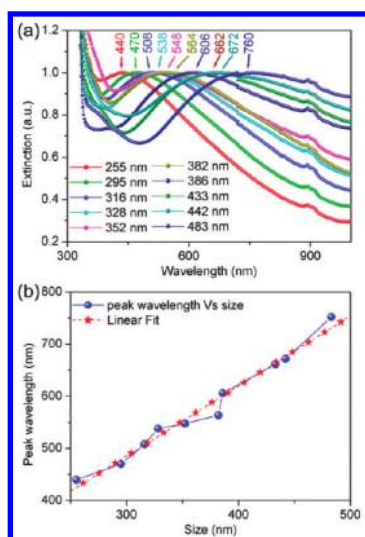


Figure 6. (a) Normalized UV-vis extinction spectra of products formed by PLICN with different laser fluences and irradiation times depicted in Figure 3a. (b) Relationship between extinction peaks and average sizes of spherical particles.

for particles with different sizes d_p , and then the specific laser fluence that results in the full melting of particles with given sizes can be determined. To make such a Mie calculation, we input together with laser wavelength λ and particle diameter d_p two other parameters: refractive index and extinction coefficient of TiO_2 , which were defined experimentally.¹⁷

$$Q_{\text{abs}}(\lambda, d_p) = J\sigma_{\text{abs}}^{\lambda}(d_p) \quad (2)$$

Figure 5 depicts our calculation result (355 nm), in which both larger and smaller particles need high energy to start melt and full melt, similar to the case of CuO system.¹¹ For particles with size larger than 250 nm, it can be observed that higher laser fluence will result in the full melting of much larger particles; that is, the size of spherical droplet increases at higher laser fluence, and this could explain why experimentally increasing the laser fluence leads to the increase of the sizes of resultant spherical particles (Figure 3a). At a given laser fluence, spherical particles cannot grow by fusion with nearby nanoparticles endlessly because the maximum of the full-melted particles is already defined by the input laser fluence. However, for the case of raw materials with higher concentration, the same input laser fluence will only result in start melting instead of full melting of the larger agglomerate, thus leading to the formation of irregular shaped product (Figure 3d). For the using of second harmonic laser (532 nm), a much higher fluence threshold is obtained for start melting and full melting according to our calculation (Figure S4), as compared to that of the third harmonic; thus a much higher laser fluence is required for spherical particles formation (Figure 3b). One important reason that the liquid medium affects the formation of the spherical particles is that the refractive index of liquid medium is one parameter that determines the cross section of $\sigma_{\text{abs}}^{\lambda}$, which determines the laser fluence required for the full melting of particles.

Figure 6a presents the UV-vis extinction spectra of the obtained TiO_2 spherical particles of different sizes depicted in Figure 3a. For an easy comparison of the absorption peaks shift, we normalize each extinction spectrum by fixing the maximum extinction value in visible light range as 1. Absorption below

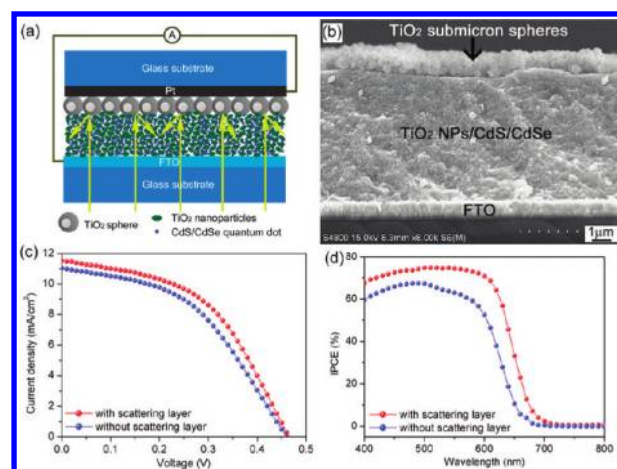


Figure 7. (a) Schematic illustration of a scattering layer of TiO_2 hollow spheres involving QDSSCs. (b) Cross-section FESEM image of a TiO_2 sphere-covered QD-sensitized TiO_2 mesoporous electrode. (c) Solar-to-electric efficiency and (d) IPCE spectra of QDSSCs with and without a scattering layer of TiO_2 hollow spheres.

410 nm, corresponding to a bandgap energy of 3.02 eV, represents the intrinsic optical absorption of rutile TiO_2 . The extinction peaks of the resultant particles clearly demonstrate a red shift from 440 to 760 nm with increased particle size; meanwhile, the extinction peaks gradually broaden. For nanoparticles, both the red shift and the peak-broadening of the band-edge absorption can result from the size increase of the nanoparticles.¹⁸ However, the red shift of the extinction peaks indicated in Figure 6a is not a shift of band-edge absorption because the extinction peaks of the resultant TiO_2 spheres are much higher than 410 nm. One reasonable explanation is that resonant scattering occurs when the particle size is comparable to the wavelength of the incident light.¹⁹ This also explains why the peak positions demonstrate a red shift: larger particles scatter light with a longer wavelength.²⁰ The broadening of the peak width is assumed to come from the wide size dispersity of the resultant submicrometer spheres. Figure 6b demonstrates the relationship between the extinction peaks and the average particle sizes, which is roughly linear. A slope of 1.5 can be obtained from the linear fit indicated in Figure 6b. Thus, particles with an average size of d_p can result in resonant scattering peaked at $1.5d_p$, which is smaller than that of the theoretical result of $2d_p$.²⁰ The reason is not yet clear, but one possible reason may be the wide size distribution of the spherical particles.

In a typical QDSSC configuration, thickness and light penetration depth are very important for constructing efficient solar cell device. Thin film device has an advantage for the efficient charge transfer of photogenerated carriers and diffusion of redox couples in electrolyte, but the visible light cannot be fully absorbed by QDs in thin film layer. The remnant light reaches to the counter electrode, leading to an insufficient utilization of the input sunlight. Inspired by the light scattering of TiO_2 submicrometer spheres, we introduced a scattering layer of TiO_2 spheres (average size 483 nm) in QDSSCs. As demonstrated in Figure 7a, TiO_2 -sphere-covered QD-sensitized TiO_2 mesoporous film is sealed in sandwich cells using Pt-coated glass and FTO glass as counter electrodes. After sunlight passes through the QD-sensitized TiO_2 mesoporous film, the remnant light is scattered back for secondary absorption of QDs due to the

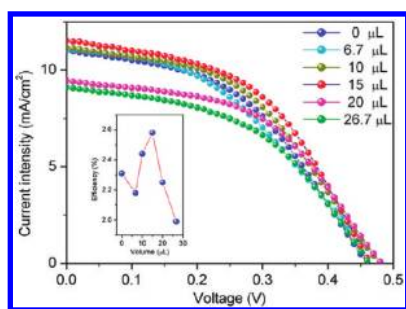


Figure 8. C–V characteristics of the solar cells based on QDSSCs coated with TiO₂ scattering layers prepared by dropping concentrated TiO₂ colloidal sphere solution (2.8 mg/mL) with different volumes. Inset is the scattering-layer-thickness-dependent efficiency of QDSSCs.

light-scattering effect. Figure 7b depicts the cross section of the TiO₂ sphere-covered QDSSC, in which a 6 μm thick mesoporous TiO₂ film sensitized by CdS/CdSe QDs is covered with a 1.5 μm layer of TiO₂ spheres. The resulting QDSSCs with a TiO₂ sphere scattering layer were characterized by measuring current–voltage characteristics in an aperture area of 0.25 cm² under standard AM 1.5 simulated sunlight. It was found in our experiments that the current–voltage (CV) characteristics of the prepared QDSSCs were much sensitive to the measuring procedures (see Figure S5), in which refreshing electrolyte and increasing illumination time can gradually enhance the solar cell performance, which is in agreement with previous report.²¹ Therefore, each CV curve presented in this Article was obtained by numerous refreshing electrolyte and increasing CV-curve measuring times to get the finally best performance. For each condition, at least three cells were tested at each condition to validate the obtained trends. Typical current–voltage curves for the samples with and without a scattering layer are depicted in Figure 7c. The TiO₂ electrode without a scattering layer had a short-circuit current density of 11 mA cm^{−2} and an energy conversion efficiency of 2.31%; the TiO₂ electrode with a scattering layer achieved a current density of 11.5 mA cm^{−2} and a conversion efficiency of 2.58%. This result indicates a 10% increase in conversion efficiency. The incident photon-to-current conversion efficiency (IPCE) spectra from both materials were further collected to compare the photovoltaic performance of TiO₂ electrodes with and without a scattering layer. A solar cell with a scattering layer had much higher IPCE (Figure 7d). In addition, the IPCE spectrum of a solar cell with a scattering layer had a tail broadened to the infrared area, which originated from the broad light scattering of TiO₂ submicrometer spherical particles.

Further studies reveal that the adopted volumes of TiO₂ colloidal sphere solution dropped on a QD-sensitized TiO₂ mesoporous film electrode affect solar cell efficiency (see Figure 8). As different volumes of the adopted colloidal solutions result in scattering layers of different thicknesses, it can be clearly observed that too thick scattering layer coating (for cases of 20 and 26.7 μL) will result in the decrease of short-circuit photocurrent density. As is seen in the inset in Figure 8, when the scattering layer of TiO₂ spheres was introduced, with the increasing of thickness of scattering layer, the resulted solar-to-electric conversion efficiency first drops (6.7 μL), then increases to the highest value (15 μL), and finally drops again. Further structural characterization of the QDSSCs reveals that the whole coverage of the coating layer over the surface of QDSSCs cannot

Table 1. Comparison of Short-Circuit Photocurrent Density (J_{sc}), Open-Circuit Voltage (V_{oc}), Fill Factor (FF), and Conversion Efficiency for Quantum-Dots-Sensitized Solar Cells with and without Scattering Layers

volume (μL)	J_{sc} (mA cm ^{−2})	V_{oc} (mV)	FF	η (%)
0	11.02	0.46	0.45	2.31
10	11.12	0.49	0.45	2.44
15	11.49	0.47	0.48	2.58
20	9.38	0.49	0.49	2.25
26.7	9.08	0.47	0.47	1.97

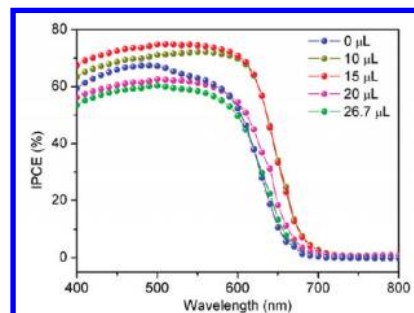


Figure 9. IPCE of the solar cells based on QDSSCs with and without TiO₂ scattering layers.

be formed until using more than 10 μL of TiO₂ submicrometer spheres colloidal solutions (Figure S6); therefore, we consider that the using of 6.7 μL of coating solution cannot cause an effective back scattering. On the other hand, the utilization of the scattering layer could obstruct the charge transfer to the redox couples (S^{2-}/S) in electrolyte solution. The above two reasons could explain why for the 6.7 μL case the efficiency drops as compared to that of QDSSCs with no coating. Table 1 provides a detailed comparison of the photovoltaic characteristics of the QDSSCs with those of coated by scattering layers, in which we ignored the data of QDSSCs coated by 6.7 μL of TiO₂ spheres solution because it cannot provide an effective back scattering. Previous studies on QDSSCs reveal that the V_{oc} values are sensitive with the adopted quantum dot species and their chemical bath deposition cycles, which could result in a 0.1–0.2 V difference.²² In the present study, as seen in Table 1, the open-circuit voltages (V_{oc}) of the different QDSSCs are around the same value, which could also be observed from Figure 8, indicating that for the construction of those QDSSCs in our experiments, the procedure of CdS/CdSe quantum dots preparation is in a good manner of reproducibility.

The scattering effect of the coating layers can be clearly observed in Figure 9, which shows the IPCE spectra as a function of wavelength for the QDSSCs coated with and without TiO₂ submicrometer spheres. It can be seen that all of the spectra from QDSSCs with scattering layers exhibit broadened tails to the infrared region, as compared to that of without scattering layer (the blue dotted curve), arising from the scattering effect of the submicrometer spheres layer. Careful examination reveals that the thickness of the scattering layer also determines the scattering effect at infrared region: with the increase of the layer thickness, the IPCE value at the range of 650–680 nm first enhanced and then decreased, indicating that the too thick scattering layer is not good for the effective scattering. In addition, the too thick scattering layer is also not favorable for the obtaining of high

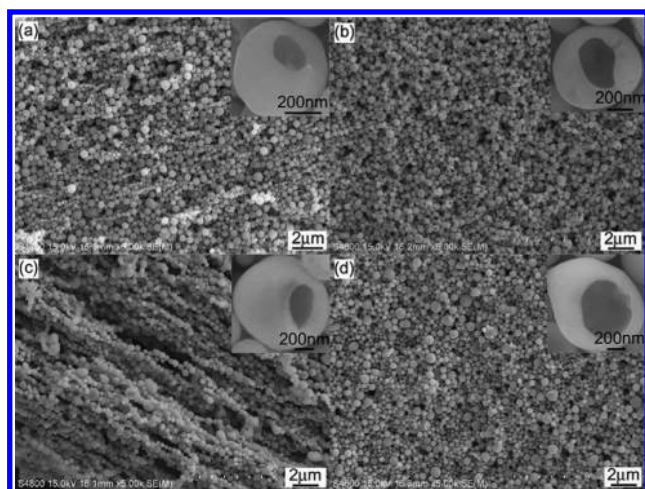


Figure 10. FESEM images of products after PLICN of (a) Fe, (b) NiO, (c) Ni, and (d) Co_3O_4 .

current intensity, which is in agreement with the tendency shown in Figure 8.

Both the CV curves and the IPCE spectra shown above demonstrated that use of different volumes of the adopted colloidal solutions results in an optimized solar cell performance, and this phenomenon can be qualitatively explained by a balance between the backscattering-enhanced light trapping and the barrier of charge transfer to the redox couples (S^{2-}/S) in electrolyte solution caused by the scattering layer: a thick scattering layer has a strong backscattering effect but also strongly blocks the photoinduced electron transfer to the electrolyte, and vice versa. Besides, we assume that the broad size distribution of TiO_2 facilitates wide-range visible-light harvesting and that its single-crystalline feature facilitates photoinduced electron transfer. Further, our preliminary calculation indicates that hollow spheres could demonstrate an enhanced scattering effect as compared to those of solid spheres with comparable sizes (see Figure S7), indicating the potential applications of the coating layer using hollow spheres. It is highly anticipated that efficiency can be further improved in future work by tuning sphere size in the scattering layer and optimizing the preparation of quantum dots.

Importantly, the synthesis method presented in this study for hollow spheres fabrication was revealed to be suitable for synthesizing many other metals and semiconductors (e.g., Fe, Co, Ni, Co_3O_4 , NiO, WO_3 , and Fe_2O_3) (see some typical examples in Figure 10). A similar phenomenon with TiO_2 raw nanoparticles was observed for these materials (i.e., these raw nanoparticles are also strongly agglomerated), further confirming our proposed mechanism in this Article. Therefore, one possible way to extend this approach to fabricating a much broader range of hollow materials is to induce agglomeration of raw nanoparticles. However, one disadvantage of the present technique is the incapability of the void size control because we consider that the voids come from the gas randomly existing between the nanoparticles, which is currently beyond our control.

In summary, we have demonstrated a facile laser process for producing single-crystalline TiO_2 hollow spheres at room temperature. Rapid quenching after instantaneous melting of TiO_2 agglomerates or nanoparticles is necessary for forming TiO_2 spherical particles. The diffusion analogous to the Kirkendall

effect after the surface melting of TiO_2 congeries is assumed to be responsible for forming hollow spheres. Experimental parameters (e.g., laser wavelength, laser fluence/irradiation time, liquid medium, and concentration of starting materials) were found important for synthesizing TiO_2 spherical particles. A wide-range size-related extinction of TiO_2 spherical particles was observed and further used to increase the light-harvesting capability of QDSSCs, and a current 10% improvement has been achieved. This method was also found suitable for fabricating other size-tailored semiconductor hollow spheres. We thus believe that our study is of great use for extensive research on inorganic single-crystalline hollow spheres.

■ ASSOCIATED CONTENT

S Supporting Information. Characterizations, theoretical calculation, and solar cell results. This material is available free of charge via the Internet at <http://pubs.acs.org>.

■ AUTHOR INFORMATION

Corresponding Author

hqwang@issp.ac.cn; koshizaki.naoto@aist.go.jp

■ ACKNOWLEDGMENT

This work was partially supported by Grants-in-Aid for Scientific Research (B) (20360340) and on Innovative Areas "Frontier science of interactions between plasmas and nano-interfaces" from the Ministry of Education, Culture, Sports, Science and Technology, Japan. This work was also partially supported by the National Natural Science Foundation of China (no. 10904145 and no. 10974203) and the Anhui Natural Science Foundation (no. 090414188).

■ REFERENCES

- (1) (a) Zhou, Y.; Antonietti, M. *J. Am. Chem. Soc.* **2003**, *125*, 14960–14961. (b) Li, Y.; Sasaki, T.; Shimizu, Y.; Koshizaki, N. *J. Am. Chem. Soc.* **2008**, *130*, 14755–14762. (c) Hu, X.; Gong, J.; Zhang, L.; Yu, J. C. *Adv. Mater.* **2008**, *20*, 4845–4850. (d) Deng, H.; Li, X.; Peng, Q.; Wang, X.; Chen, J.; Li, Y. *Angew. Chem., Int. Ed.* **2005**, *44*, 2782–2785. (e) Zhang, Q.; Chou, T. P.; Russo, B.; Jenekhe, A. A.; Cao, G. *Angew. Chem., Int. Ed.* **2008**, *47*, 2402–2406. (f) Duan, H.; Wang, D.; Sobal, N. S.; Giersig, M.; Kurth, D. G.; Möhwalld, H. *Nano Lett.* **2005**, *5*, 949–952.
- (2) (a) Mathlowitz, E.; Jacob, J. S.; Jong, Y. S.; Carino, G. P.; Chickering, D. E.; Chaturvedl, P.; Santos, C. A.; Vijayaraghavan, K.; Montgomery, S.; Bassett, M.; Morrell, C. *Nature* **1997**, *386*, 410–414. (b) Zhang, W. M.; Hu, J. S.; Guo, Y. G.; Zheng, S. F.; Zhong, L. S.; Song, W. G.; Wan, L. J. *Adv. Mater.* **2008**, *20*, 1160–1165. (c) Park, J. H.; Jung, S. Y.; Kim, R.; Park, N. G.; Kim, J.; Lee, S. S. *J. Power Sources* **2009**, *194*, 574–579. (d) Shchukin, D. G.; Ustinovich, E. A.; Sukhorukov, G. B.; Möhwalld, H.; Sviridov, D. V. *Adv. Mater.* **2005**, *17*, 468–472. (e) Shchukin, D. G.; Möhwalld, H. *Adv. Funct. Mater.* **2007**, *17*, 1451–1458. (f) Shchukin, D. G.; Köhler, K.; Möhwalld, H. *J. Am. Chem. Soc.* **2006**, *128*, 4560–4561. (g) Gong, Y.; Gao, M.; Wang, D.; Möhwalld, H. *Chem. Mater.* **2005**, *17*, 2648–2653.
- (3) (a) Caruso, F.; Caruso, R. A.; Möhwalld, H. *Science* **1998**, *282*, 1111–1114. (b) Yang, M.; Ma, J.; Zhang, C. L.; Yang, Z. Z.; Lu, Y. F. *Angew. Chem., Int. Ed.* **2005**, *44*, 6727–6730. (c) Yu, J. G.; Yu, X. X. *Environ. Sci. Technol.* **2008**, *42*, 4902–4907. (d) Zhong, Z.; Yin, Y.; Gates, B.; Xia, Y. *Adv. Mater.* **2000**, *12*, 206–209. (e) Kim, S. W.; Kim, M.; Lee, W. Y.; Hyeon, T. *J. Am. Chem. Soc.* **2002**, *124*, 7642–7643. (f) Liang,

H. P.; Zhang, H. M.; Hu, J. S.; Guo, Y. G.; Wan, L. J.; Bai, C. L. *Angew. Chem., Int. Ed.* **2004**, *43*, 1540–1543.

(4) (a) Hu, Y.; Chen, J. F.; Chen, W. M.; Lin, X. H.; Li, X. L. *Adv. Mater.* **2003**, *15*, 726–729. (b) Dinsmore, A. D.; Hsu, M. F.; Nikolaides, M. G.; Marquez, M.; Bausch, A. R.; Weitz, D. A. *Science* **2002**, *298*, 1006–1009. (c) Li, Y. S.; Shi, J. L.; Hua, Z. L.; Chen, H. R.; Ruan, M. L.; Yan, D. S. *Nano Lett.* **2003**, *3*, 609–612. (d) Peng, Q.; Dong, Y.; Li, Y. *Angew. Chem., Int. Ed.* **2003**, *42*, 3027–3030. (e) Yang, H. G.; Zeng, H. C. *Angew. Chem., Int. Ed.* **2004**, *43*, 5206–5209. (f) Buchold, D. H. M.; Feldmann, C. *Nano Lett.* **2007**, *7*, 3489–3492.

(5) (a) Yin, Y.; Rioux, R. M.; Erdonmez, C. K.; Hughes, S.; Somorjai, G. A.; Alivisatos, A. P. *Science* **2004**, *304*, 711–714. (b) Zeng, H. C. *J. Mater. Chem.* **2006**, *16*, 649–662. (c) Liang, X.; Xu, B.; Kuang, S. M.; Wang, X. *Adv. Mater.* **2008**, *20*, 3739–3744.

(6) (a) Zheng, Q.; Zhou, B. X.; Bai, J.; Li, L. H.; Jin, Z. J.; Zhang, J. L.; Li, J. H.; Liu, Y. B.; Cai, W. M.; Zhu, X. Y. *Adv. Mater.* **2008**, *20*, 1044–1049. (b) Shchukin, D. G.; Caruso, R. A. *Chem. Mater.* **2004**, *16*, 2287–2292. (c) Hosono, E.; Fujihara, S. B.; Imai, H.; Honma, I.; Masaki, I.; Zhou, H. S. *ACS Nano* **2007**, *1*, 273–278. (d) Li, Y.; Fang, X. S.; Koshizaki, N.; Sasaki, T.; Li, L.; Gao, S. Y.; Shimizu, Y.; Bando, Y.; Golberg, D. *Adv. Funct. Mater.* **2009**, *19*, 2467–2473. (e) Li, Y.; Sasaki, T.; Shimizu, Y.; Koshizaki, N. *Small* **2008**, *4*, 2286–2291.

(7) (a) Kondo, Y.; Yoshikawa, H.; Awaga, K.; Murayama, M.; Mori, T.; Sunada, K.; Bandow, S.; Iijima, S. *Langmuir* **2008**, *24*, 547–550. (b) Koo, H.-J.; Kim, Y. J.; Lee, Y. H.; Lee, W. I.; Kim, K.; Park, N.-G. *Adv. Mater.* **2008**, *20*, 195–199. (c) Ding, S.; Chen, J. S.; Wang, Z.; Cheah, Y. L.; Madhavi, S.; Hu, X.; Lou, X. W. *J. Mater. Chem.* **2011**, *21*, 1677–1680. (d) Liu, S.; Yu, J.; Jaroniec, M. *J. Am. Chem. Soc.* **2010**, *132*, 11914–11916. (e) Kong, L.; Lu, X.; Bian, X.; Zhang, W.; Wang, C. *J. Solid State Chem.* **2010**, *183*, 2421–2425.

(8) Liu, Z.; Miyauchi, M.; Uemura, Y.; Cui, Y.; Hara, K.; Zhao, Z.; Sunahara, K.; Furube, A. *Appl. Phys. Lett.* **2010**, *96*, 233107–1–3.

(9) Hu, M.; Poulikakos, D.; Grigoropoulos, C. P.; Pan, H. J. *Chem. Phys.* **2010**, *132*, 164504–1–11.

(10) Wang, H. Q.; Pyatenko, A.; Kawaguchi, K.; Li, X. Y.; Swiatkowska-Warkocka, Z.; Koshizaki, N. *Angew. Chem., Int. Ed.* **2010**, *49*, 6361–6364.

(11) (a) Ishikawa, Y.; Shimizu, Y.; Sasaki, T.; Koshizaki, N. *Appl. Phys. Lett.* **2007**, *91*, 161110–1–3. (b) Ishikawa, Y.; Feng, Q.; Koshizaki, N. *Appl. Phys. A: Mater. Sci. Process.* **2010**, *99*, 797–803. (c) Wang, H. Q.; Koshizaki, N.; Li, L.; Jia, L. C.; Kawaguchi, K.; Li, X. Y.; Pyatenko, A.; Swiatkowska-Warkocka, Z.; Bando, Y.; Golberg, D. *Adv. Mater.* **2011**, *23*, 1865–1870.

(12) (a) Hoffmann, M. R.; Martin, W.; Choi, W.; Bahnemann, D. W. *Chem. Rev.* **1995**, *95*, 69–96. (b) Liu, P.; Cai, W.; Fang, M.; Li, Z.; Zeng, H.; Hu, J.; Luo, X.; Jing, W. *Nanotechnology* **2009**, *20*, 285707–1–6.

(13) (a) Pyatenko, A.; Yamaguchi, M.; Suzuki, M. *J. Phys. Chem. C* **2009**, *113*, 9078–9085. (b) Pyatenko, A.; Yamaguchi, M.; Suzuki, M. *J. Phys. Chem. C* **2009**, *111*, 7910–7917.

(14) Wang, Y.; Xia, Y. *Nano Lett.* **2004**, *4*, 2047–2050.

(15) Yang, G. W. *Prog. Mater. Sci.* **2007**, *52*, 648–698.

(16) JANAF thermochemical Tables 1974 supplement.

(17) Mosaddeq-ur-Rahman, M.; Yu, G.; Krishna, K. M.; Soga, T.; Watanabe, J.; Jimbo, T.; Umeno, M. *Appl. Opt.* **1998**, *37*, 691–697.

(18) Viswanatha, R.; Sapra, S.; Satpati, B.; Satyam, P. V.; Dev, B. N.; Sarma, D. D. *J. Mater. Chem.* **2004**, *14*, 661–668.

(19) Zhang, Q.; Chou, T. P.; Russo, B.; Jenekhe, S. A.; Cao, G. *Adv. Funct. Mater.* **2008**, *18*, 1654–1660.

(20) Stamatakis, P.; Palmer, B. R.; Salzman, G. C.; Bohren, C. F.; Allen, T. B. *J. Coat. Technol.* **1990**, *62*, 95–98.

(21) Giménez, S.; Mora-Seró, I.; Macor, L.; Guijarro, N.; Lana-Villarreal, T.; Gómez, R.; Diguna, L. J.; Shen, Q.; Toyoda, T.; Bisquert, J. *Nanotechnology* **2009**, *20*, 295204–1–6.

(22) (a) Lee, Y.-L.; Lo, Y.-S. *Adv. Funct. Mater.* **2009**, *19*, 604–609. (b) Kamat, P. V. *J. Phys. Chem. C* **2008**, *112*, 18737–18753.